Artificial magnetic granularity effects on patterned epitaxial YBa$_2$Cu$_3$O$_{7-x}$ thin films

E. Bartolomé,[1,2] A. Palau,[1] J. Gutiérrez,[1] X. Granados,[1] A. Pomar,[1] T. Puig,[1] X. Obradors,[1] V. Cambel,[3] J. Soltys,[3] D. Gregusova,[3] D. X. Chen,[4,5] and A. Sánchez[4]

[1]*Institut de Ciència de Materials de Barcelona–CSIC, Campus UAB, 08193 Bellaterra, Spain*
[2]*Escola Universitaria Salesiana de Sarrià, Passeig Sant Joan Bosco 74, 08017 Barcelona, Spain*
[3]*Institute of Electrical Engineering, Slovak Academy of Sciences, Dubravska Cesta 9, 84104 Bratislava, Slovakia*
[4]*Grup d'Electromagnetisme, Departament of Física, Universitat Autònoma de Barcelona, 08193 Bellaterra, Spain*
[5]*ICREA, Passeig Lluis Companys 23, 08010 Barcelona, Spain*
(Received 4 June 2007; revised manuscript received 24 July 2007; published 12 September 2007)

An artificial "multigranular" YBCO thin film has been prepared by patterning a network of gridlines, emulating the current-restricting behavior of grain boundaries. This model system allowed us to investigate the magnetic effects of granularity and current percolation problem, having control on the geometry, number of grains, and ratio of inter-to-intragrain critical-current density reduction, J_c^{GB}/J_c^G. The dc magnetization cycle at 5 K showed a peak shift to a positive applied magnetic field value, typically ascribed to granularity. ac measurements performed up to very high driving ac magnetic fields show that ac losses are dominated by dissipation over the whole grain boundary network, whereas the contribution of individual grains cannot be resolved. A high-resolution (<5 μm) Hall-probe imaging system has been used to visualize the evolution of the magnetization distribution with a cycled applied magnetic field (at 4.2 and 77 K), and deduce maps of the intragranular and intergranular currents by solving the inverse problem. Quantitative information about the J_c^{GB} and J_c^G magnetic field dependence and the spatial distribution of J_c^G are presented and discussed.

I. INTRODUCTION

The implementation of high-T_c superconductors (HTSs) in large-scale applications requires achieving high critical-current density values. Inherent granularity is one of the main factors limiting the flow of large supercurrents through these materials, and consequently, different texturing processes have been developed in order to obtain bulks and tapes with large parallel grains, strong junctions, and planar supercurrents.

In the context of HTS tapes, second generation, YBa$_2$Cu$_3$O$_7$ (YBCO) coated conductors with a high biaxial texture can be nowadays achieved by means of the ion beam assisted deposition (IBAD)[1,2] or rolling assisted biaxially textured substrate (RABiTS)[3,4] techniques, although an in-plane granular microstructure induced by the substrate is still present.[5] Since the critical-current density decreases strongly with the grain misalignment angle,[6] $J_c^{GB}(\theta)$, transport current flows over these conductors in a percolative way through the network of low-angle grain boundaries (GBs). This behavior has been clearly identified by magneto-optical (MO) imaging[5] and transport[7] measurements. Current percolation has been treated by several authors before.[5,6,8,9] Several two-dimensional (2D) models have been developed to predict the complex current circulating patterns across polycrystalline samples.[10–13] The flux penetration through samples patterned into different granular configurations has been studied by MO, showing the effect of this granularity onto the magnetization loops.[14,15] Transport[16–18] and inductive[19–21] methodologies have been applied to determine the grain J_c^G and intergrain J_c^{GB}; understanding the interaction between these two is one of the most interesting topics at present.[22–24]

In this paper, we investigate experimentally the current percolation problem in an artificially "granular" YBCO film prepared by photolithography, which can become a very useful model system. A patterned network of gridlines imitates the current flow restricting behavior of GBs. The inter-to-intragrain critical-current density ratio J_c^{GB}/J_c^G at each GB can be varied by tuning the spacing between the gridline holes. The magnetic effects associated with the granular geometry can be thus discriminated and studied in a controlled way, because the shape, size, number of grains, and J_c^{GB}/J_c^G ratio can be tuned *ad hoc*. Thus, this approach paves the way for a systematic investigation of the basic physical effects associated with the disordered granular geometry of coated conductors.

We have analyzed the effects of granularity on the magnetic behavior of a "multigranular" YBCO thin film combining three complementary magnetometry techniques. First, dc magnetic measurements have been carried out to study distinctive features on the magnetic hysteretic cycles associated with granularity, on the basis of previous works on coated conductors, which demonstrated that granularity manifests in anomalous $M(H)$ cycles.[21] Second, ac susceptibility has been applied to investigate the grain and GB contributions to the ac losses. This technique has shown to be useful for the study of polycrystalline samples[25] and coated conductors[26] where the dissipation due to different GB networks could even be identified.[27]

The above techniques allow only inferring the granular effects on the *macroscopic* magnetic behavior. In order to investigate the *local* superconducting properties, a magnetic flux imaging technique, such as Hall-probe microscopy[28–31] or MO imaging[32,33] is required. The latter offers an unmatched spatial resolution (1 μm); however, samples can be explored only in a small magnetic field range (<0.2 T) due to the saturation of the ferromagnetic garnet. In contrast, Hall-probe imaging under magnetic fields up to 1 T has
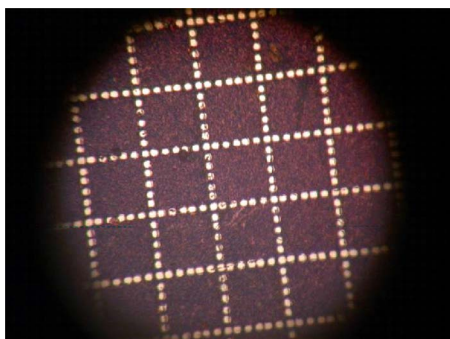
FIG. 1. (Color online) Micrograph of the artificial 21×21 multigranular sample. The grain size is 200×200 μm^2. The small holes defining the GBs are 30 μm size, spaced by 10 μm (J_c^{GB}/J_c^G =0.25).

proved to be a powerful tool for the investigation of the local magnetization and the local vs long-range critical currents, for instance, in the study of granular[34–36] and porous[37,38] superconductors.

In this work, we have used a high-resolution, low-temperature, Hall-probe imaging system to actually visualize the granular magnetic distribution at different applied magnetic fields up to 0.8 T of our multigranular sample. By using a computational inverse problem solver ("CARAGOL"[39]), current maps showing the intragranular current loops and percolative current circulation have been determined. Quantitative information about J_c^G and J_c^{GB}, and their magnetic field and temperature dependences are presented and discussed.

II. EXPERIMENT

An artificial multigranular sample was prepared as follows. An epitaxial YBCO thin film of thickness $t=300$ nm was deposited on a 4.5×4.5 mm^2 LAO single-crystal substrate by standard pulsed laser deposition. The system used a KrF-excimer laser with an energy density of 2 J/cm^2, running at 10 Hz, with a deposition rate of 0.07 nm/pulse. The deposition was carried out in an oxygen atmosphere of 0.23 mbar with the substrate at 775 °C, and was followed by an oxygenation process at 1 bar while cooling down the sample from 550 °C to room temperature.

Subsequently, a squared network of artificial GBs, defining 21×21 grains of 200×200 μm^2 size, was patterned by standard 10 μm optical photolithography (Fig. 1). Each GB consisted of an array of 30 μm size holes, 10 μm apart from each other, so that the critical-current density reduction at each GB was set to be $J_c^{GB}/J_c^G=0.25$. According to the $J_c^{GB}(\theta)$ angle dependence found from bicrystal studies,[40,41,8] this reduction would be equivalent to that produced by a real GB with a misorientation of $\theta \approx 10°$. We would like to note that in real granular systems, grain dimensions are considerably smaller than in our artificial granular system (~ 2 μm for IBAD and ~ 30 μm for RABiTS coated conductors), and GBs contain nonsuperconducting dislocation cores several nanometers apart, instead of micrometers. However, this has

no influence for studying the current percolation problem and magnetic effects purely associated with the granular geometry, while our model system allows a much more accurate control of the GB network configuration. On the other hand, our system will not be able to replicate other effects related to the GB electronic structure or pinning of GB vortices, which should be further investigated with other kinds of experiments.

The dc magnetometry measurements were carried out in a Quantum Design superconducting quantum interference device (SQUID) equipped with a 7 T superconducting coil. ac susceptibility curves in temperature sweep (50–92 K) were measured with a Quantum Design physical property measurement system, at driving ac amplitudes between $\mu_0 H_{ac}$ =0.01 and 1.5 mT applied perpendicular to the substrate, at frequency $f=1111$ Hz, and zero dc magnetic field. In addition, ac measurements at very high driving magnetic fields (up to $\mu_0 H_{ac}=40$ mT) at 77 K, at frequencies between 90 and 2500 Hz, were performed with a homemade susceptometer.[42]

The magnetic Hall-probe scanning measurements were performed in a system described in Ref. 43. The sensor is a homemade 5 μm bar patterned on GaAs/AlGaAs heterostructure, which is scanned above the sample surface by two stepping motors. The advantage of this system is to combine a high spatial resolution (<5 μm), good magnetic field resolution (1×10^{-7} T/Hz$^{1/2}$), and large scanning area (7 $\times 25$ mm^2), with the possibility of working in a flow cryostat at temperatures between 4.2 and 300 K, under magnetic fields up to ± 0.8 T, in this case applied perpendicular to the sample surface. The distance between the sensor and the sample surface can be adjusted by means of a piezoelectric element in steps of ± 5 μm. The usual "zoom-in" procedure consisted of progressively approaching the sensor to the sample surface during a scan, until contact was achieved, and then raising the sensor a distance h above the sample. Because it was virtually impossible to adjust the sample surface exactly parallel to the scanning plane, measurements were usually done at rather "safe" flying distances h ≈ 10–50 μm to avoid probe damaging. The precise value of h could then be calibrated *a posteriori* with the help of the inversion program, as described in Sec. IV B.

III. dc-ac MAGNETOMETRY RESULTS

A. dc magnetometry results

Figure 2 shows for comparison the SQUID-measured $M(H)$ saturated cycles at 5 K, before (bold circles) and after (open circles) the patterning process defining the granular structure. The effects of granularity result in an anomalous cycle, with a magnetization peak on the reverse curve at a positive value of the applied magnetic field ($\mu_0 H_{peak}^{sat}$ ≈ 25 mT) for the granular sample, as compared with the standard cycle (peak at $H_{peak}^{sat}=0$) found for the nongranular sample. This peak-shift effect, earlier observed in coated conductors,[44] has been found to be a typical signature of granularity, which can be explained by means of the effect of the return magnetic field from the grains into the GBs.[21] The
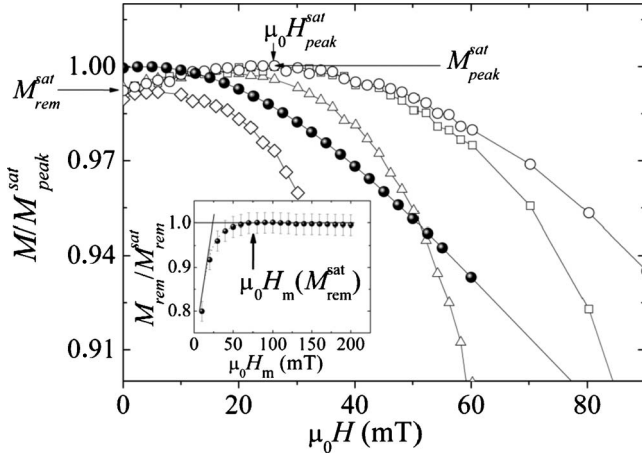
FIG. 2. SQUID determined magnetization cycles normalized by the peak magnetization value $M/M_{\text{peak}}^{\text{sat}}$ vs applied magnetic field at 5 K, before (bold) and after (open) patterning the granular structure. Cycles measured for different values of the maximum applied magnetic field $\mu_0 H_m$: ($\diamond$) 60 mT, ($\triangle$) 80 mT, ($\square$) 110 mT, and ($\bigcirc$) 140 mT. The inset shows the saturation of the remanent magnetization for $\mu_0 H_m > 80$ mT.

local magnetic field at each GB is the vectorial sum of the applied magnetic field H and the return magnetic field H_{return} coming from the trapped magnetic field at each grain:

$$H^{\text{GB}} = H - H_{\text{return}}. \tag{1}$$

Hence, the magnetization peak appears when $H^{\text{GB}} = 0$, i.e., when $H \sim H_{\text{return}}$.

We would like to mention that a peak-shift effect has been also reported in (nongranular) YBCO thin films when a significant amount of porosity was present.[45] In that case, pores act in a similar way as the artificial holes in our sample, restricting the flow of percolative currents through the sample.

Figure 2 (open symbols) shows magnetic hysteresis loops measured up to different values of the maximum applied magnetic field $\mu_0 H_m$ for the patterned sample. The inset represents the evolution of the remanent magnetization normalized to its saturation value $M_{\text{rem}}/M_{\text{rem}}^{\text{sat}}$ for increasing values of $\mu_0 H_m$. As discussed in Ref. 21 the maximum applied field $\mu_0 H_m$ correlates directly with the grain magnetic field penetration, and thus the maximum applied magnetic field that saturates the remanent magnetic moment corresponds to the full penetration magnetic field of the grains, $H_m(M_{\text{rem}}^{\text{sat}}) = 2H_G^*$, in our case ~ 80 mT.

The intergranular J_c^{GB} (5 K) has been determined from the irreversible magnetization of the patterned cycle. The size of the grains was designed such that the magnetic moment associated to the grain current loops was negligible compared to the magnetic moment of the large percolative current, $m_G \ll m_{\text{GB}}$. Hence, the saturated value of the magnetization at the peak $M_{\text{peak}}^{\text{sat}}$ corresponds to the magnetic moment of currents flowing across the GBs, and serves to determine the J_c^{GB} at $H_{\text{loc}} = 0$ under the critical-state, thin film disk approximation as

$$J_c^{\text{GB}} = \frac{3M_{\text{peak}}^{\text{sat}}|_{\text{patt}}}{R}, \tag{2}$$

where $R \sim 2.8$ mm is the sample radius, yielding $J_c^{\text{GB}} = 2.9 \times 10^{10}$ A/m². The magnetic field dependence of the intergrain critical-current density was determined from the reverse saturated magnetization branch as $J_c^{\text{GB}}(H) = 3M(H)/R$. Similarly, the intragranular J_c^{G} has been obtained from the magnetization cycle before patterning as

$$J_c^{\text{G}} = \frac{3M_{\text{non-patt}}}{R}, \tag{3}$$

yielding $J_c^{\text{G}}(5 \text{ K}) = 1.1 \times 10^{11}$ A/m² in self-field. In summary, the SQUID-determined inter-to-intragrain critical-current density ratio in the granular sample at 5 K is $J_c^{\text{GB}}/J_c^{\text{G}} = 0.25$, in good agreement with the ratio *a priori* expected from the dimensions defined by photolithography.

B. ac susceptibility results

Figure 3(a) shows the real and imaginary components of the ac susceptibility, χ' and χ'', measured as function of the temperature, for different values of the ac magnetic field and $f = 1111$ Hz. A single χ'' peak can be distinguished, which as we will show next, is due to GB dissipation, while the grain contribution cannot be resolved here. The expected values of the maximum ac imaginary component, χ''_{peak}, for cylinders of different aspect ratio $2R/t$ were calculated in Ref. 27, using an energy minimization model.[46] According to that, the observed single peak, $\chi''^{\text{GB}}_{\text{peak}} = 1752$, corresponds to dissipation in a region of radius $R \approx 2.6$ mm comparable to the sample size, and thus it is due to ac losses in the GB network. The estimated grain contribution, assuming the squared patterned grains to be cylinders of equivalent radius $a \sim 112$ μm, is $\chi''^{\text{G}}_{\text{peak}} = 76$, which is negligibly small compared to the GB peak. Thus, in these range of temperatures and magnetic fields, the dynamic flux penetration into the granular sample occurs through the GB network, and qualitatively, the sample presents a critical-state-like behavior associated with the whole sample area.

Figure 3(b) shows the χ' and χ'' curves measured as a function of the ac driving magnetic field $\mu_0 H_a$ at 77 K. Here, also, a single, broad χ'' peak can be distinguished, up to the very high magnetic field measured (40 mT), arising mainly from ac losses at the artificial GB network. Dissipation produced by individual grains cannot be resolved due to their small size, though presumably their contribution causes the asymmetric widening of the $\chi''^{\text{GB}}_{\text{peak}}$ peak at high magnetic fields.

From the χ'' curves, we have determined the temperature dependence of the inter- and intragrain critical-current densities by means of the equation[47]

$$J_c^{\text{GB}}(T_{\text{peak}}^{\text{GB}}) = \frac{2H_{\text{ac}}}{1.94t}, \tag{4}$$

valid for cylinders of aspect radius $2R/t > 100$. This condition holds in our case, $2R/t \approx 16900$. It can be observed (Fig. 4) that the J_c^{GB} values obtained from ac susceptibility
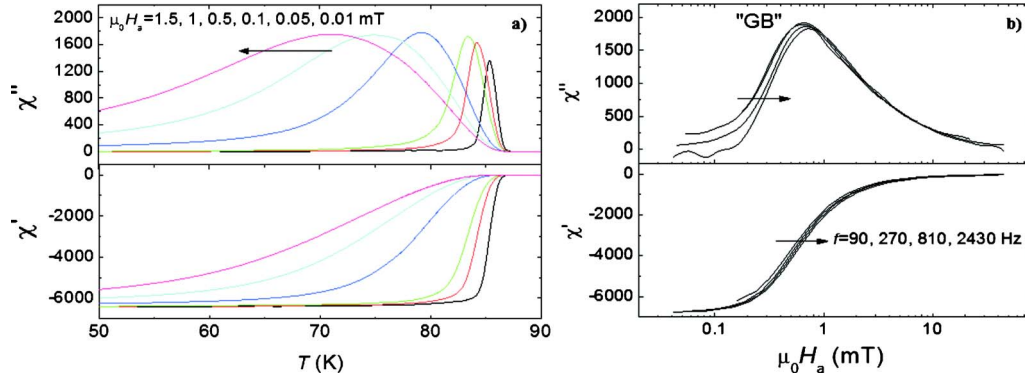
FIG. 3. (Color online) (a) Temperature dependence of the real χ' and imaginary χ'' components of the ac susceptibility (SI units) for $\mu_0 H_{ac} = 0.01$, 0.05, 0.1, 0.5, 1.0, and 1.5 mT at $f = 1111$ Hz; (b) ac magnetic field dependence of the real χ' and imaginary χ'' components of the ac susceptibility for $f = 90$, 270, 810, and 2430 Hz at 77 K.

measurements correspond well to those calculated from dc magnetometry.

IV. HALL-PROBE MAGNETIC IMAGING

A. Simulated magnetization distribution

The remanent magnetization of our multigranular sample was simulated within the Bean model in 2D with the self-developed program "TRAZACORRIENTES®."[48] Basically, the program simulates the pattern of induced supercurrents appearing in a $m \times m$ meshed superconducting sample containing nonsuperconducting areas, in this case the holes defining the artificial GBs. A zero-field-cooled (ZFC) process is simulated, after which an applied magnetic field is gradually increased in steps of NH_{min} until reaching saturation at $H_{max} = N_{max}H_{min}$. For simplicity, we set the local critical-current density $J_c = J_c^G \equiv 1$ by definition. Because J_c is field independent in our approximation, the simulated current distribution in the remanence is a mirror pattern to that in the fully penetrated state. Assigning a color scale to the formed N-current

loops, a picture of the distributed magnetization is obtained.

As shown in Fig. 5, the simulated remanent pattern of our 21×21 granular sample consists of a global critical-state pyramid, caused by the circulation of the percolating intergrain current over the whole sample, on top of which, an array of small pyramids, due to the formation of closed current loops inside the grains can be identified.

B. Magnetic Hall-probe imaging results

Local magnetization measurements performed by Hall-probe imaging are presented next; since J_c increases with decreasing T, scans were made at 4.2 K in order to enhance flux contrast and be able to distinguish more clearly the granular structure.

The B_z map in the remanence after a field-cooled (FC) process looked similar to the critical-state pattern (Fig. 5) predicted by the simulation. Figure 6(a) shows a 600 $\times 600$ μm^2 area of the remanent map, measured close to the sample border with a resolution of 10 μm. The trapped field at the 200×200 μm^2 grains and the GB network can be clearly distinguished. The high spatial resolution of this imaging system allowed even resolving the fine magnetic struc-
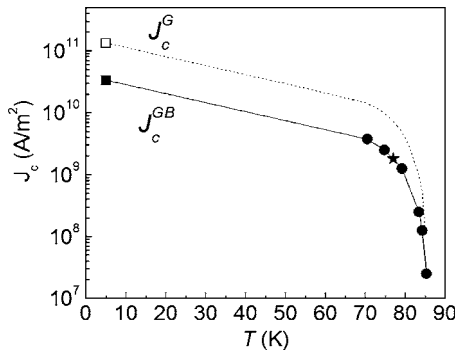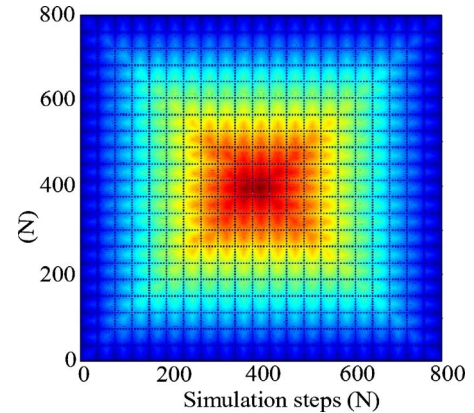

FIG. 4. Temperature dependence of the intergranular (bold) and intragranular (open) critical-current densities determined from SQUID dc magnetometry (squares), T sweep ac susceptibility (circles), and H_a sweep ac susceptibility at 77 K (star). The $J_c^G(T)$ dependence (dashed line) is estimated as $J_c^G(T)/f$, where the GB transparency $f = 0.25$ is settled by the photolithography dimensions and is therefore temperature independent.

FIG. 5. (Color online) Magnetization in the remanence simulated by the program TRAZACORRIENTES® for the 21×21 granular sample with a critical-current density reduction at each GB of 0.25.
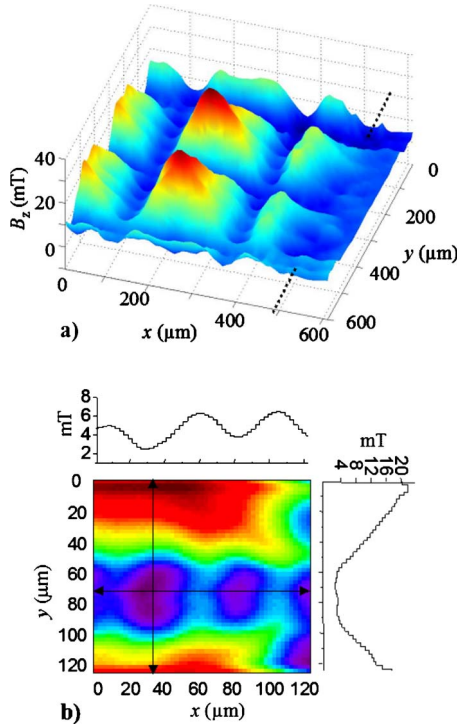
FIG. 6. (Color online) (a) B_z map in the remanence after a fc process of a region close to the sample border (indicated by the dotted line), measured with a resolution of 10 μm; (b) detail of the magnetic structure at one of the artificially patterned "GBs," measured with resolution 2.5 μm. Cross sections along the GB (top figure) and transversal to the GB (right figure) are shown.

ture formed at the artificial "GBs" [Fig. 6(b)]. The magnetic distribution exhibits depression in size and periodicity coinciding with that of the patterned hole arrays defining the GBs.

In order to study further the dynamics of the granular magnetization, we measured the B_z maps at different applied magnetic fields up to 0.8 T along a hysteretic cycle, after a ZFC process. So as to have reasonable scanning times, just $\frac{1}{4}$ of the sample with a resolution of 25 μm was measured. Then, a reasonable picture of the magnetization over the whole sample could be obtained by using the fourfold symmetry of the sample. Figure 7 shows as an example the scanned B_z map at a magnetic field μ_0H=43.5 mT on the initial magnetization curve. The granular magnetic structure and preferential flux penetration through the square network of artificial GBs can be clearly observed. Note that, due to a small inclination of the sample surface with respect to the scanning plane, the flux pattern is sharper at the right side than at the bottom side of the sample.

Figure 7(a) depicts a cross section of the overall, background "magnetization," measured by tracing a B_z profile on top of a "GB," whose slope is directly proportional to J_c^{GB}. On the other hand, B_z profiles crossing either a line [Fig. 7(b)] or column [Fig. 7(c)] of grains show the periodic 200 μm size magnetization peaks, with a slope given by J_c^{G}.

Finally, note that macroscopic information can be also extracted from the Hall-probe in-field measurements. By integrating the local magnitude $B_z(x,y,\mu_0H)$-μ_0H over the
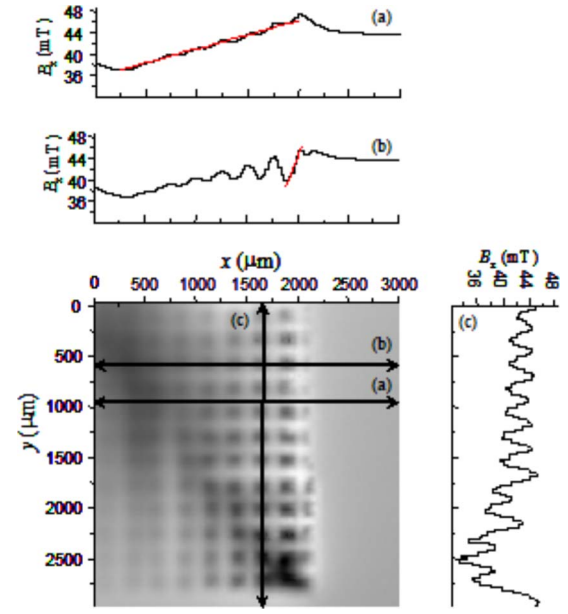

FIG. 7. (Color online) B_z Hall-probe image of approximately $\frac{1}{4}$ of the sample surface, at an applied magnetic field μ_0H=43.5 mT on the initial magnetization curve, at 4.2 K (ZFC). Also shown, B_z profile along (a) a line of grains, (b) an artificial GB, and (c) a column of grains close to the sample border.

whole scanned area S, we determined the hysteresis cycle, directly proportional to $M(H)$:[37]

$$\frac{1}{S}\int_S (B_z - \mu_0H) = [B_z - \mu_0H](H) \propto M(H). \quad (5)$$

Figure 8 shows that the so obtained magnetization cycle $[B_z$-$\mu_0H](H)$ exhibits a maximum peak on the return branch
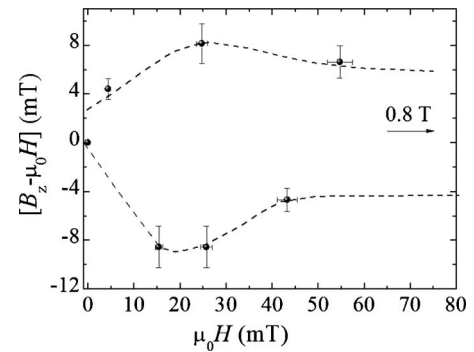

FIG. 8. Integrated "magnetization" $[B_z$-$\mu_0H]$ vs applied magnetic field μ_0H cycle determined from Hall-probe magnetometry at 4.2 K.

of the hysteresis cycle at a positive value, in agreement with the SQUID measurements shown in Sec. III A.

C. Local critical-current density determination

One of the most important aspects of granularity that could be tackled by Hall-probe imaging was the local study of the inter- and intragrain critical-current densities. The distribution of critical-current densities was determined from the Hall-probe magnetization maps by solving back the Biot-Savart law using the Fourier transform based inversion solver program (CARAGOL[39]).

For computing the current distribution, we used magnetization maps $B_z(x,y,\mu_0H)$-μ_0H, obtained by scanning $\frac{1}{4}$ of the sample and then forming a magnetic image of the whole sample by symmetry. Figure 9(a) shows, for instance, the so reconstructed magnetization map at an applied magnetic field of $\mu_0H=25$ mT. We had to use magnetic images of the complete sample and not just scans of a sample fraction, because the presence of discontinuities in the B_z field map at the image borders would result in erroneously computed values of J_c.

For the inversion, the distance between the sample surface and the Hall probe, h, needs to be accurately determined. To do so, we computed with CARAGOL the current maps for different distances h; using them as input, we recalculated the $B_z(h)$ maps by forward application of the Biot-Savart law, and compared the latter with the original measured B_z maps. For the actual distance h, the original and recalculated maps differed only by 5%.

The computed critical-current density distributions $J_c(x,y,H)$ were decomposed in their Cartesian coordinates J_x, J_y to facilitate the visualization of the current loops and determination of J_c^{GB} and J_c^G. Figures 9(b) and 9(c) illustrate the $J_x(x,y)$ and $J_y(x,y)$ maps found from the magnetization map measured at $\mu_0H=25$ mT on the return curve, at a flying distance $h=30$ μm [Fig. 9(a)].

If we consider the general critical-state roof shape formed over the sample, the currents in the opposite triangular roof sectors run parallel to the sample borders, e.g., those in the upper and lower triangles of Fig. 9(a) flow parallel to the x axis, and $J_c(x,y)$ in those areas equals the J_x component: $J_c(x,y) \equiv [J_x(x,y),0]$. Then, the intergranular J_c^{GB} is easily determined from a profile cross sectioning the J_x map [Fig. 9(b)]; when we integrate J_x between the border and the center of the sample, the closed loop currents formed at the grains cancel each other, and only J_c^{GB} remains

$$J_c^{GB}(H) = \frac{1}{L/2}\int_0^{L/2} J_y(x,y,H)dx. \quad (6)$$

Figure 10 (open symbols) shows the obtained magnetic field dependence of the intergranular critical-current density, $J_c^{GB}(H)$. Note that, in accordance with the characteristic $M(H)$ cycle previously presented (Figs. 2 and 8), the J_c^{GB} at the positive magnetic field $\mu_0H=25$ mT is larger than at 0 mT, which is explained by the effect of the return magnetic field from the grains into the GBs, as described in Sec. III A.

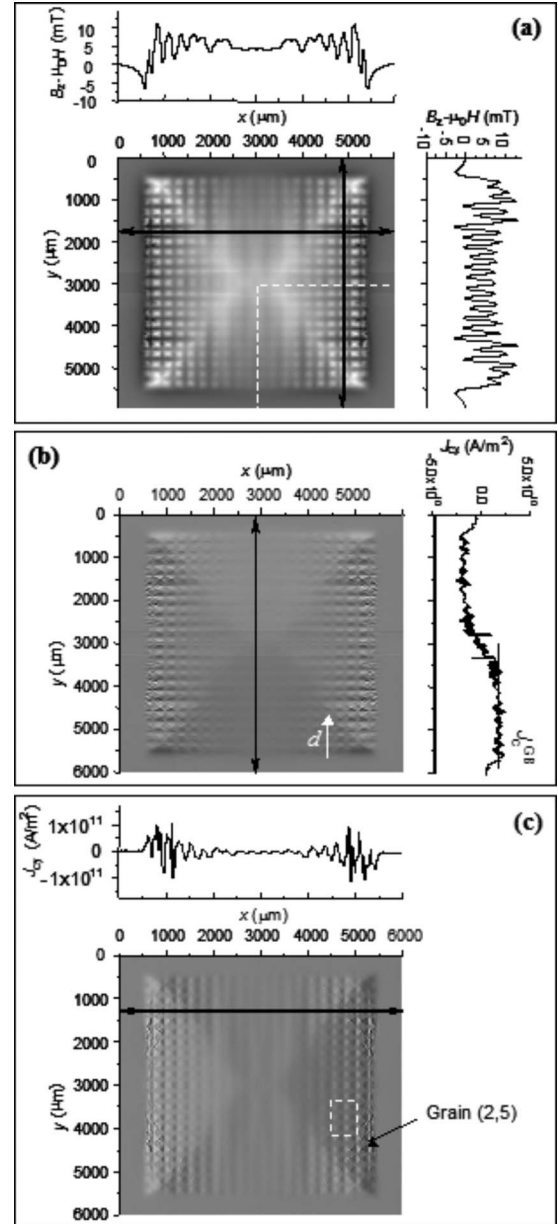Most interestingly, the intragranular J_c^G as a function of the grain position within the sample and the applied mag-

FIG. 9. (a) "Reconstructed" $[B_z$-$\mu_0H]$ map at $\mu_0H=25$ mT on the return branch of the hysteresis cycle, $T=4.2$ K (ZFC). Also shown, $[B_z$-$\mu_0H]$ profile along a row of grains (top figure) and along a column of grains (right figure), indicated by black arrow lines; (b) calculated $J_x(x,y)$ component of the critical-current density. The white arrow indicates the column of grains used for the $J_c^G(d)$ determination. Right figure: $J_{cy}(y)$ profile across the sample center (black arrow) from which J_c^{GB} is determined; (c) calculated $J_y(x,y)$ critical-current density component. Top figure: $J_{cy}(x)$ profile along a line of grains.

netic field can be additionally determined with this technique. Figure 11 illustrates the intragrain critical-current density determination for six grains positioned within the sample, as indicated in Fig. 9(c). A small rooflike critical-state pattern is formed at each grain, and it holds that $J_c(x,y) \equiv [J_x(x,y),0] \equiv [0,J_y(x,y)]$. Then, J_c^G can be evaluated as the maximum of the J_y-component profile crossing
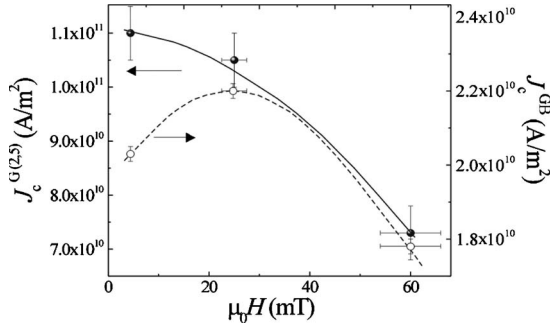
FIG. 10. Magnetic field dependence of $J_c^{GB}(H)$ (○) and $J_c^G(H)$ (●) at 4.2 K. The intragranular J_c^G has been determined for a particular grain (2,5) indicated in Fig. 9(b).

each grain. (The J_x-component may of course equally be used.)

The $J_c^G(H)$ dependence with the magnetic field can then be determined for each particular grain, as exemplified in Fig. 10, where the $J_c^G(H)$ of grain (2,5) indicated in Fig. 9(b) is shown, compared to the intergranular $J_c^{GB}(H)$ curve.

Note that for each applied magnetic field H, the intragranular J_c^G may vary significantly from grain to grain due to the dependence of J_c^G on the local internal magnetic, having a spatial distribution $H_i(x,y)$ over the sample. In order to estimate the importance of this effect, we have determined J_c^G as a function of the position d of the grain with respect to the sample border. The following consideration was utilized
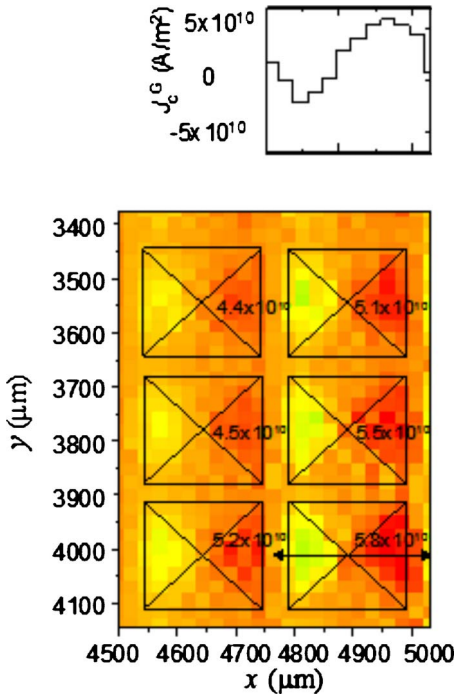

FIG. 11. (Color online) Determination of the position dependent intragranular $J_c^G(x,y)$ at $\mu_0 H = 25$ mT for six grains [their position within the sample is indicated in Fig. 9(c)]. Top figure: J_x profile across a single grain from which J_c^G is determined as the value at the maximum. The J_c^G value at each grain is given in A/m^2.
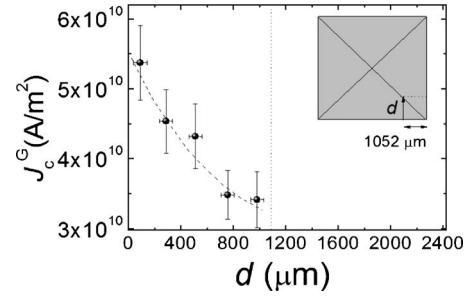

FIG. 12. Dependence of the intragranular critical-current density with the position of the grain respect to the sample border, $J_c^G(d)$, as sketched in the inset.

here: the sample surface was slightly inclined in the $(x,y =$const$)$ plane with respect to the scanning plane, as can be noticed from the gradient in the field intensity out of the sample (see Fig. 7). In order to ensure that the $J_c^G(d)$ dependence was given by the internal magnetic field spatial distribution and not by the inclination effect, $J_c^G(d)$ was determined along grains in rows parallel to y axis [see Fig. 9(b)], for which the sample-to-Hall-probe distance was invariant. Figure 12 shows the decreasing $J_c^G(d)$ relationship so obtained; the curve, in fact, reflects the $J_c(H_i)$ internal magnetic field dependence, where H_i increases as we get deeper into the sample.

The intragrain spatial distribution and its dependence on the magnetic field constitute important information that cannot be extracted from the dc magnetometry, which averages J_c^G over the sample.

Finally, a similar analysis to the one presented at 4.2 K was carried out at 77 K, allowing us to obtain J_c^G and J_c^{GB} at that temperature. The results, not shown here, were qualitatively the same as those at 4.2 K. However, it is worthwhile to summarize and make some final remarks about the J_c^{GB}/J_c^G results at different temperatures from the different magnetometries.

The J_c^{GB}/J_c^G ratio determined at 4.2 K, from Hall-probe microscopy (~ 0.2) and dc magnetometry (0.25), is approximately equal to the ratio obtained at 77 K by Hall-probe measurements (~ 0.2). This result shows consistency of both determination techniques. Furthermore, J_c^{GB}/J_c^G was proved to be temperature independent, in agreement with the fact that the inter-to-intragranular current ration was defined *a priori* by the photolithography. As the material has a unique intrinsic $J_c^G(T)$ dependence, we proved that J_c^{GB} is defined by the patterning as a fraction of J_c^G, and therefore is also independent of temperature. The situation would be different in a genuine granular sample such as a coated conductor, where J_c^{GB} depends not only on the geometrical restriction of the GB but also on the GB electronic properties and GB vortices, so that J_c^G and J_c^{GB} are ruled by different vortex pinning mechanisms and could eventually present different temperature dependencies.

V. CONCLUSIONS

A model granular system, prepared by photolithography patterning an YBCO thin film, has been used to study the

magnetic effects associated with granularity and the current percolation problem in a controlled configuration. The macroscopic effects of granularity have been measured by dc magnetometry and ac susceptibility. As a consequence of the granular structure, the $M(H)$ cycle at 5 K measured by dc magnetometry exhibits a peak shift to a positive applied magnetic field value, which is explained by the effect of the return magnetic field from the grains into the GBs. ac susceptibility measurements performed both as function of temperature and magnetic field (up to 40 mT) show that dissipation is associated with currents running over the whole sample through the GB network, while losses due to currents at individual grains cannot be distinguished. A homemade Hall-probe imaging system with a high spatial resolution ($<5~\mu$m) has been used to visualize the granular distribution of the magnetization and follow its evolution along a cycled magnetic field up to 0.8 T, at 4.2 and 77 K. By solving the inverse problem, we have determined local critical-current density maps, $J_c(x,y,H)$, from which J_c^{GB} and J_c^{G} have been deduced. The use of this local magnetometry technique has allowed us to determine the grain-to-grain variation of J_c^{G} within the sample.

We anticipate that the use of structured, artificial "GBs," allowing to tune in a controlled manner the grain number, size, and rate of critical-current density reduction per GB, opens the way for a systematic investigation of the effects of granularity on the magnetic properties of superconductors.

[1] Y. Ijima, K. Onabe, N. Futaki, N. Tanabe, N. Sadakata, O. Cono, and Y. Ikeno, J. Appl. Phys. **74**, 1905 (1993).

[2] J. Dzick, J. Wiesmann, J. Hoffmann, K. Heinemann, F. García-Moreno, A. Isaev, H. C. Freyhardt, and W. Lechner, IEEE Trans. Appl. Supercond. **9**, 2248 (1999).

[3] D. P. Norton, A. Goyal, J. D. Budai, D. K. Christen, D. M. Kroeger, E. D. Specht, Q. He, B. Saffian, M. Paranthaman, C. E. Klabunde, D. F. Lee, B. C. Sales, and F. A. List, Science **274**, 755 (1996).

[4] B. de Boer, J. Eickemeyer, N. Reger, L. Fernández, J. Richter, B. Holzapfel, L. Schultz, W. Prusseit, and P. Berberich, Acta Mater. **49**, 1421 (2001).

[5] D. M. Feldmann, J. L. Reeves, A. A. Polyanskii, G. Kozlowski, R. R. Biggers, R. M. Nekkanti, I. Maartense, M. Tomsic, P. Barnes, C. E. Oberly, T. L. Peterson, S. E. Babcock, and D. C. Larbalestier, Appl. Phys. Lett. **77**, 2906 (2000).

[6] H. Hilgenkamp and J. Mannhart, Rev. Mod. Phys. **74**, 485 (2002).

[7] D. M. Feldmann, D. C. Larbalestier, D. T. Verebelyi, W. Zhang, Q. Li, G. N. Riley, R. Feenstra, A. Goyal, D. F. Lee, M. Paranthaman, D. M. Kroeger, and D. K. Christen, Appl. Phys. Lett. **79**, 3998 (2001).

[8] D. T. Verebelyi, D. K. Christen, R. Feenstra, C. Cantoni, A. Goyal, D. F. Lee, M. Paranthaman, P. N. Arendt, R. F. DePaula, J. R. Groves, and C. Prouteau, Appl. Phys. Lett. **76**, 1755 (2000).

[9] L. Fernández, B. Holzapfel, F. Schindler, B. de Boer, A. Attenberger, J. Hanisch, and L. Schultz, Phys. Rev. B **67**, 052503 (2003).

[10] J. E. Evetts, M. J. Hogg, B. A. Glowacki, N. A. Rutter, and V. N. Tsaneva, Supercond. Sci. Technol. **12**, 1050 (1999).

[11] B. Holzapfel, L. Fernández, F. Schindler, B. De Boer, N. Reger, J. Eickemeyer, P. Berberich, and W. Prusseit, IEEE Trans. Appl. Supercond. **11**, 3872 (2001).

[12] N. A. Rutter, B. A. Glowacki, and J. E. Evetts, Supercond. Sci. Technol. **13**, L25 (2000).

[13] E. D. Specht, A. Goyal, and M. Kroeger, Supercond. Sci. Technol. **13**, 592 (2000).

[14] M. R. Koblischka, L. Pust, A. Galkin, P. Nalevka, M. Jirsa, T. H. Johansen, H. Bratsberg, B. Nilsson, and T. Claeson, Phys. Rev. B **59**, 12114 (1999).

[15] M. Jirsa, V. Yurchenko, A. V. Bobyl, T. H. Johansen, D. V. Shantsev, and R. Wördenweber, Physica C **404**, 200 (2004).

[16] D. C. van der Laan and J. W. Ekin, Appl. Phys. Lett. **90**, 052506 (2007).

[17] L. Civale, B. Maiorov, A. Serquis, J. O. Willis, J. Y. Coulter, H. Wang, Q. X. Jia, P. N. Arendt, J. L. MacManus-Driscoll, M. P. Maley, and S. R. Foltyn, Appl. Phys. Lett. **84**, 2121 (2004).

[18] A. Diaz, L. Mechin, P. Berghuis, and J. E. Evetts, Phys. Rev. Lett. **80**, 3855 (1998).

[19] K. H. Muller, C. Andrikidis, H. K. Liu, and S. X. Dou, Phys. Rev. B **50**, 10218 (1994).

[20] S. Tonies, A. Vostner, and H. W. Weber, J. Appl. Phys. **92**, 2628 (2002).

[21] A. Palau, T. Puig, X. Obradors, and Ch. Jooss, Phys. Rev. B **75**, 054517 (2007).

[22] A. Gurevich and L. D. Cooley, Phys. Rev. B **50**, 13563 (1994).

[23] C. Joos and J. Albrecht, Z. Metallkd. **93**, 1065 (2002).

[24] A. Palau, T. Puig, J. Gutierrez, X. Obradors, and F. de la Cruz, Phys. Rev. B **73**, 132508 (2006).

[25] F. Gömory, Supercond. Sci. Technol. **10**, 523 (1997).

[26] D. X. Chen, E. Pardo, A. Sánchez, A. Palau, T. Puig, and X. Obradors, Appl. Phys. Lett. **85**, 5646 (2004).

[27] T. Puig, A. Palau, X. Obradors, E. Pardo, C. Navau, A. Sánchez, C. Jooss, K. Guth, and H. C. Freyhardt, Supercond. Sci. Technol. **17**, 1283 (2004).

[28] S. J. Bending, Adv. Phys. **48**, 449 (1999).

[29] G. K. Perkins, Supercond. Sci. Technol. **14**, 685 (2001).

[30] R. B. Dinner, M. R. Bearley, and K. A. Moler, Rev. Sci. Instrum. **76**, 103702 (2005).

[31] J. K. Gregory, Rev. Sci. Instrum. **73**, 3515 (2002).

[32] A. A. Polyanskii, A. Gurevich, J. Jiang, Larbalestier, S. L.

Bud'ko, D. K. Finnemore, G. Lapertot, and P. C. Canfield, Supercond. Sci. Technol. **14**, 811 (2001).

[33] L. Gozzelino, F. Laviano, D. Botta, A. Chiodoni, R. Gerbaldo, G. Ghigo, E. Monticone, C. Portesi, and E. Mezzetti, Supercond. Sci. Technol. **16**, 199 (2003).

[34] S. Iliescu, S. Sena, X. Granados, E. Bartolomé, T. Puig, X. Obradors, M. Carrera, J. Amoró, S. Krakunovska, and T. Habisreuther, IEEE Trans. Appl. Supercond. **13**, 3136 (2003).

[35] E. Bartolomé, X. Granados, V. Cambel, J. Fedor, P. Kovac, and I. Husek, Supercond. Sci. Technol. **18**, 1135 (2005).

[36] B. Bozzo, S. Iliescu, E. Bartolomé, A. Palau, X. Granados, T. Puig, X. Obradors, J. Amorós, and M. Carrera, Supercond. Sci. Technol. **18**, 1227 (2005).

[37] E. Bartolomé, X. Granados, T. Puig, X. Obradors, E. S. Reddy, and G. J. Schmitz, Phys. Rev. B **70**, 144514 (2004).

[38] E. Bartolomé, X. Granados, T. Puig, X. Obradors, E. S. Reddy, and S. Kracunovska, IEEE Trans. Appl. Supercond. **15**, 2775 (2005).

[39] M. Carrera, J. Amorós, X. Obradors, and J. F. Fontcuberta, Supercond. Sci. Technol. **16**, 1187 (2003).

[40] N. F. Heinig, R. D. Redwing, I. F. Tsu, A. Gurevich, J. E. Nordman, S. E. Babcock, and D. C. Larbalestier, Appl. Phys. Lett. **69**, 577 (1996).

[41] Z. G. Ivanov, P. A. Nilsson, D. Winkler, J. A. Alarco, T. Claeson, E. A. Stepantsov, and A. Y. Tzalenchuk, Appl. Phys. Lett. **59**, 3030 (1991).

[42] D. X. Chen, Meas. Sci. Technol. **15**, 1195 (2004).

[43] V. Cambel, J. Fedor, D. Gregušová, P. Kováč, and I. Hušek, Supercond. Sci. Technol. **18**, 417 (2005).

[44] A. Palau, T. Puig, X. Obradors, E. Pardo, C. Navau, A. Sánchez, A. Usoskin, H. C. Freyhardt, L. Fernández, B. Holzapfel, and R. Feenstra, Appl. Phys. Lett. **84**, 230 (2004).

[45] A. Pomar, J. Gutiérrez, A. Palau, T. Puig, and X. Obradors, Phys. Rev. B **73**, 214522 (2006).

[46] A. Sanchez and C. Navau, Phys. Rev. B **64**, 214506 (2001).

[47] J. R. Clem and A. Sanchez, Phys. Rev. B **50**, 9355 (2004).

[48] E. Bartolomé, F. Gömory, X. Granados, T. Puig, and X. Obradors, Supercond. Sci. Technol. **18**, 388 (2005).